Author/s:
Mohankumar, M;Fernandes, S;Cavalieri, F;Cortez-Jugo, C;Caruso, F

Title:
Ultrasound-Driven Coassembly of Anticancer Drugs into Carrier-Free Particles

Date:
2025-04-08

Citation:
Mohankumar, M., Fernandes, S., Cavalieri, F., Cortez-Jugo, C. & Caruso, F. (2025). Ultrasound-Driven Coassembly of Anticancer Drugs into Carrier-Free Particles. ACS Nano, 19 (13), pp.13366-13380. https://doi.org/10.1021/acsnano.5c01284.

Persistent Link:
https://hdl.handle.net/11343/355920

Ultrasound-Driven Coassembly of Anticancer Drugs into Carrier-Free Particles

Mirudula Mohankumar,[1] Soraia Fernandes,[1,2] Francesca Cavalieri,[2,3] Christina Cortez-Jugo,[,1] and Frank Caruso*[,1]*

[1] Department of Chemical Engineering, The University of Melbourne, Parkville, Victoria 3010, Australia

[2] School of Science, RMIT University, Melbourne, Victoria 3000, Australia

[3] Dipartimento di Scienze e Tecnologie Chimiche, Universita di Roma "Tor Vergata", Via della Ricerca Scientifica 1, 00133 Rome, Italy

*Corresponding authors. Email: fcaruso@unimelb.edu.au, christina.cortez@unimelb.edu.au

ABSTRACT

The evolution of drug resistance in tumor malignancies has necessitated advancements in anticancer drug therapy. Drug combination therapy, which can burden cancer progression at multiple target sites, has been used to address drug resistance and includes the coencapsulation of synergistic drugs within nanoparticle carriers. However, the use of organic and inorganic carriers can lead to additional material-induced safety concerns, including inflammation and antibody formation. Herein, we report an ultrasound-driven approach to combine synergistic anticancer

drugs into carrier-free particles. Venetoclax (Vtx) (as a model anticancer drug) is combined with an anticancer anthracycline drug, doxorubicin (Dox) or a myeloid cell leukemia-1 inhibitor drug (S63845) to form spherical, submicrometer-sized (~200–1000 nm in diameter) particles, consisting predominantly of the drug molecules stabilized by hydrophobic interactions. The coassembled particles, *i.e.*, nanodrugs (NDs), display comparable and two-fold higher anticancer activity than the free drugs and the mono-component NDs, respectively, in Vtx-resistant SKOV-3 cells. The coassembled NDs containing Vtx and Dox increased the survival of SKOV-3 xenograft-bearing mice by at least 6 days (~24%) in comparison with free Vtx or Vtx NDs and at least 10 days (~40%) in comparison with saline-treated mice. Microscopy analysis of tumor tissues confirmed greater tissue damage and apoptosis induced by the NDs than by the free drugs. The present findings highlight the potential of sono-driven assembled carrier-free systems in anticancer combination therapy, combining the advantages of a high surface area, slow-release particulate system with the synergistic action of multiple drugs to combat drug resistance.

KEYWORDS: nanodrugs, nanoparticles, venetoclax, tumor, combination therapy, sonochemistry

Chemotherapy that employs small molecule drugs is the most common cancer treatment,[1-3] which affects various cellular pathways to slow down and/or stop the uncontrolled proliferation of tumor cells.[4] Venetoclax (Vtx) is an example of a small molecule anticancer drug that mediates cell death by binding the Bcl-2 receptor in the mitochondria, hindering its ability to inhibit apoptosis. Vtx was approved for patient use in 2016 for the treatment of chronic lymphocytic leukemia and small lymphocytic lymphoma[5] and has been applied in combination therapy strategies to treat diverse hematological malignancies.[6-8] Despite the clinical success of Vtx, its application in monotherapy is challenged owing to increasing venetoclax resistance in cancer

cells.[7] Hence, treatment strategies often combine Vtx with other anticancer agents with multiple modes of action, *e.g.*, doxorubicin (Dox) (a DNA intercalator)[9,10] and inhibitors such as S63845 (myeloid cell leukemia-1 (Mcl1) inhibitor)[11,12] and Zanubrutinib (Bruton tyrosine kinase inhibitor), to combat drug resistance, uncontrolled disease progression, and tumor relapse, which are observed in monotherapy.[13,14]

Irrespective of the type of drug, the main challenges faced by most small molecules used in chemotherapy are nonspecificity, poor circulation, and fast systemic clearance.[15] To address these challenges, nanosized carriers (nanocarriers) have been employed to improve the circulation and pharmacokinetics of small drugs, with the liposomal formulation of Dox (Doxil) being a prime example.[16] Nanocarriers can modulate drug release and interactions with biological interfaces, and improve the stability and solubility of small drugs, particularly hydrophobic drugs, that constitute 40% of drugs on the market.[17-19] Numerous organic and inorganic nanocarriers are under investigation for the delivery of small molecules, including liposomes,[16] micelles,[20] silica,[21] and various polymer-based particles[22,23] (*e.g.*, poly(lactic-*co*-glycolic acid) nanoparticles[24]). However, some nanocarriers exhibit cellular activity and collateral toxicity (*e.g.*, cardiotoxicity, drug resistance) similar or in addition to the active small molecule.[25-28] Moreover, the encapsulating carrier may trigger undesired immunological responses to the host system owing to its physicochemical properties as well as composition.[26]

Thus, to harness the advantages of nanosized formulations, and potentially suppress the toxicity and immune responses caused by carriers, nanoparticulate carrier-free platforms composed entirely of the candidate small molecule are desirable. Diverse techniques are used to prepare carrier-free nanodrugs (NDs), including solvent precipitation,[29,30] homogenization,[31] milling,[32] template-assisted,[33] and *in vivo*[34] driven self-assembly. Different studies have demonstrated that

such carrier-free NDs display lower systemic toxicity, higher blood retention, improved drug loading,[35] and limited multidrug resistance[36] compared with either free drugs or encapsulated drugs. We previously reported the use of high-frequency ultrasound to promote the self-assembly of drugs into NDs in aqueous solvents without the use of organic solvents or toxic reagents.[25,37,38] The acoustic cavitation bubbles, produced by high-frequency (200–500 kHz) ultrasonic waves, provide a reactive surface for the transformation and self-assembly of small molecules rich in aromatic and amphiphilic groups into carrier-free particle drugs (*i.e.*, NDs).[37] Small aromatic molecules, such as *n*-benzoyl-L-tyrosine ethyl ester,[38] tryptophan,[37] phenylalanine,[39] octapeptides (made of arginine and phenylalanine),[40] tannic acid,[41] Dox,[25] and doxycycline,[42] have been transformed into NDs. However, coassembling more than one small drug molecule to study ND formation and biological activity *in vivo* remains unexplored.

Many anticancer drugs, including Vtx, Dox, and Mcl1 inhibitor, are rich in sonoresponsive aromatic and amphiphilic functional groups that can promote C–C coupling and other noncovalent interactions including, hydrogen bonding and hydrophobic interactions, under the influence of high-frequency ultrasound.[25] Herein, we report the sono-induced formation of carrier-free NDs composed of Vtx (ND_{Vtx}), as a mono-component ND, and Vtx and Dox ($ND_{Vtx+Dox}$) or Mcl1 inhibitor ($ND_{Vtx+Mcl1}$), as two-component/coassembled NDs. The stability and activity of these NDs were evaluated *in vitro* using immortalized cell lines and *in vivo* using a xenograft tumor-bearing mouse model. *In vitro*, the synthesized ND_{Vtx}, $ND_{Vtx+Dox}$, and $ND_{Vtx+Mcl1}$ retained their biological activity post sonication. *In vivo* tumor mice model studies highlighted the propensity of the coassembled $ND_{Vtx+Dox}$ to accumulate and control the progression of SKOV-3 induced tumors. Our findings demonstrate the feasibility of preparing NDs, incorporating a hydrophobic drug (*i.e.*,

Vtx) and a combination of synergistic drugs, *via* sonochemistry and provides a pathway to transforming numerous other potential drugs into NDs for use in anticancer combination therapy.

RESULTS AND DISCUSSION

Sonosynthesis and Characterization of ND_{Vtx}. Studies on the sono-transformation of small molecules into NDs have revealed that bubble formation, during acoustic cavitation, drives the formation of particulate NDs. Cavitation bubbles provide a reactive liquid–air interface for the radical-mediated dimerization (C–C coupling), hydroxylation and/or fragmentation of aromatic molecules that deposit on the bubble surface.[25,37,38] These chemical and physical processes result in the self-assembly and nano-aggregation of small molecules into uniform nanoparticles or NDs upon bubble collapse.[25,37,38]

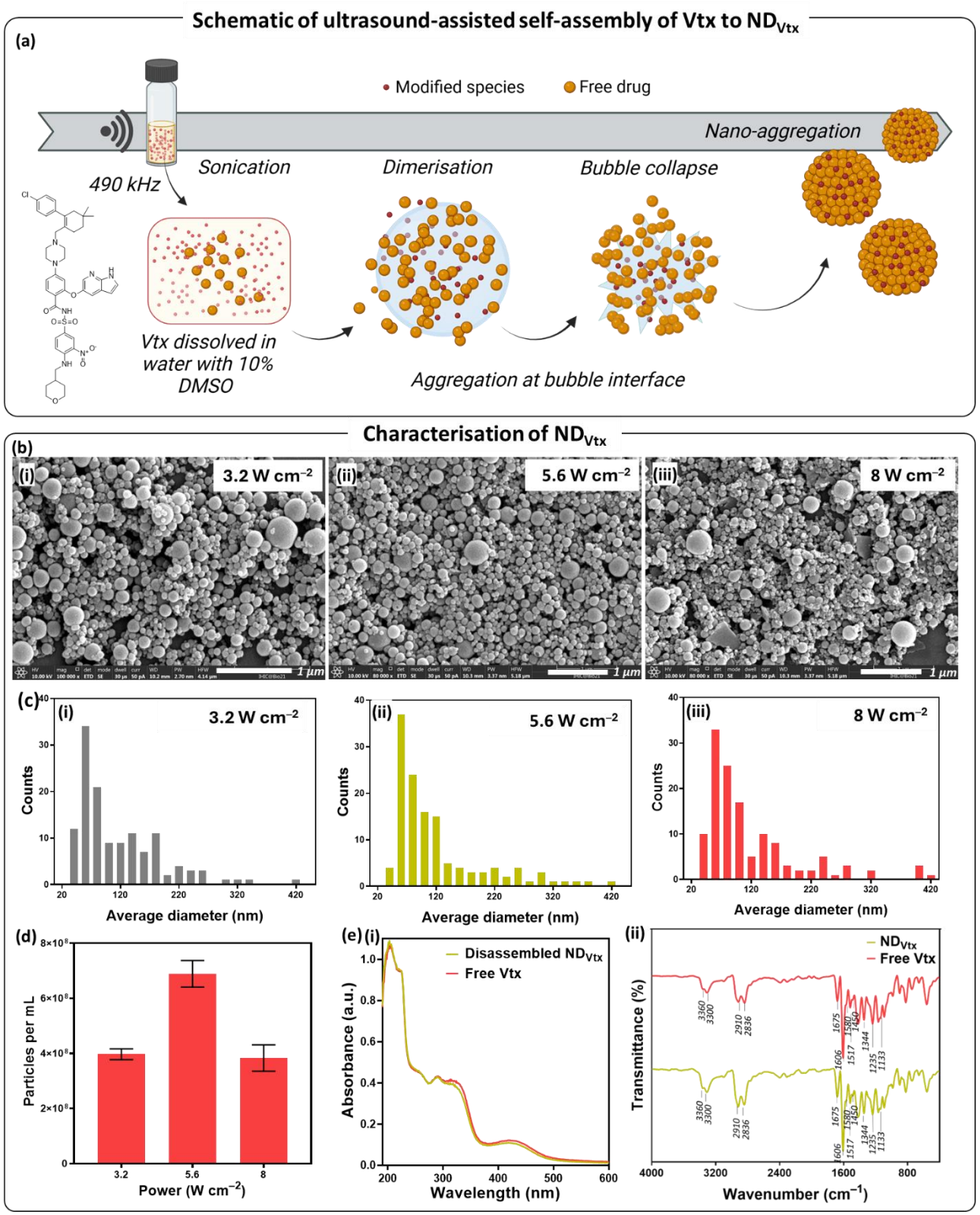

Figure 1. Ultrasound-assisted self-assembly of Vtx into ND_{Vtx}. (a) Schematic representation of the transformation of Vtx into particle nanodrugs (*i.e.*, ND_{Vtx}) using high-frequency ultrasound.

(b) SEM images of ND_{Vtx} synthesized at increasing power: (i) 3.2, (ii) 5.6, and (iii) 8 W cm^{-2} and (c) their corresponding particle size distributions, obtained from size measurement of 120 particles from the SEM images. (d) Particle concentration (as particles per mL) measured *via* NTA. Data represent mean ± standard deviation of three replicates (e) Chemical composition of ND_{Vtx}, as determined by (i) UV–vis spectroscopy and (ii) FTIR spectroscopy. Figure 1a was created with BioRender.com.

We first studied the formation of ND_{Vtx}, as illustrated in Figure 1a. To determine the effect of acoustic power on the chemical structure of Vtx and particle formation, Vtx was sonicated at a constant frequency of 490 kHz at increasing power (3.2, 5.6, and 8 W cm^{-2}) for 60 min. These parameters (frequency and time) were chosen based on previous studies that reported stable ND formation.[25,42] Scanning electron microscopy (SEM) characterization of ND_{Vtx} revealed their spherical morphology and nonhomogeneous particle size distribution (Figure 1b). The size distribution of the ND_{Vtx} measured from the SEM images ranged between 50 to 500 nm, with mean ± standard deviation diameters of 115 ± 71, 120 ± 80, and 117 ± 82 nm at 3.2, 5.6, and 8 W cm^{-2}, respectively (Figure 1c). Additionally, nanoparticle tracking analysis (NTA) revealed that using a power of 5.6 W cm^{-2} resulted in the highest particle yield, corresponding to the highest particle concentration (*i.e.*, 6.8×10^8 particles per mL) among the conditions tested (Figure 1d). Hence, owing to the higher yield and uniformity of particle morphology, a frequency of 490 kHz and a power of 5.6 W cm^{-2} were chosen as the standard ultrasound parameters for the synthesis of NDs in the subsequent studies.

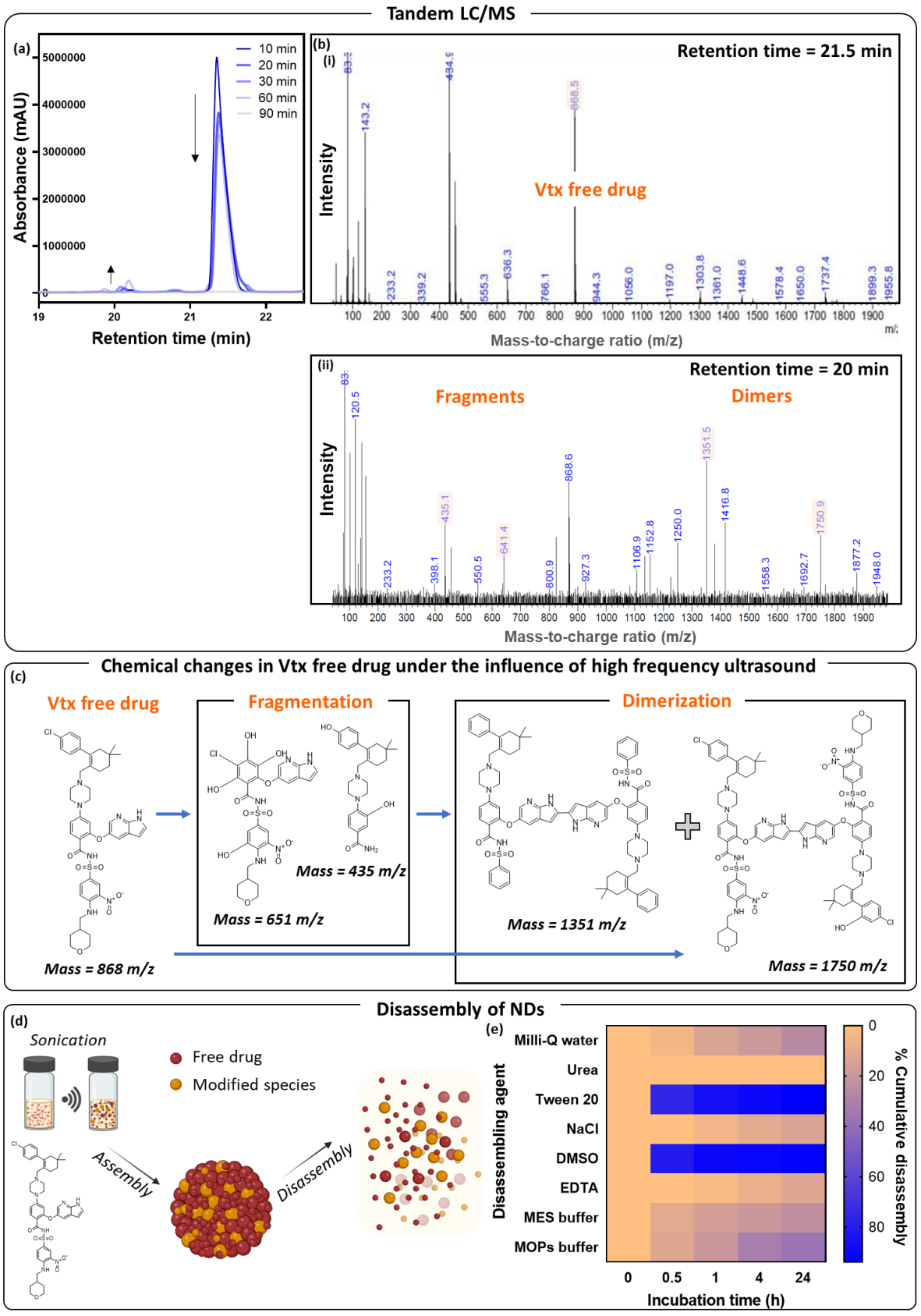
Tandem LC/MS
(a)
Absorbance (mAU)
Retention time (min)
10 min
20 min
30 min
60 min
90 min
(b)
(i)
Retention time = 21.5 min
Intensity
Vtx free drug
Mass-to-charge ratio (m/z)
(ii)
Retention time = 20 min
Fragments
Dimers
Intensity
Mass-to-charge ratio (m/z)
Chemical changes in Vtx free drug under the influence of high frequency ultrasound
(c)
Vtx free drug
Fragmentation
Dimerization
Mass = 868 m/z
Mass = 651 m/z
Mass = 435 m/z
Mass = 1351 m/z
Mass = 1750 m/z
Disassembly of NDs
(d)
Sonication
Free drug
Modified species
Assembly
Disassembly
(e)
Milli-Q water
Urea
Tween 20
NaCl
DMSO
EDTA
MES buffer
MOPs buffer
Disassembling agent
Incubation time (h)
% Cumulative disassembly

Figure 2. Characterization of the chemical composition and interactive forces within ND_{Vtx}. (a) LC pattern of sonicated Vtx showing the decrease in free Vtx (retention time at 21.5 min) with a corresponding increase in new elution peaks (between 19.5 and 20.5 min). (b) Mass spectrum of sonicated Vtx indicating the masses (*m*/*z*) of possible compounds at (i) 21.5 and (ii) 20 min. (c) Representation of the possible chemical changes occurring within Vtx during sonication, as inferred from LC/MS analysis. (d) Schematic illustration of the possible assembly of free drug and sono-modified species into NDs and their disassembly. (e) Disassembly of NDs in different reagents as a function of time. Figure 2d was created with BioRender.com.

To investigate the chemical composition of ND_{Vtx}, the NDs were disassembled in 10% dimethyl sulfoxide (DMSO) and characterized by UV–visible (UV–vis) spectroscopy. Characteristic absorption peaks of Vtx at 320 and 420 nm were observed in both the spectra of free Vtx drug and ND_{Vtx} (Figure 1e(i)). Fourier transform infrared (FTIR) spectroscopy analysis (Figure 1e(ii)) of ND_{Vtx} revealed peaks that were associated with the stretching of N–H bond (3360 and 3300 cm^{-1}), C–H bond (2910 and 2836 cm^{-1}), C=O in amide bond (1675 cm^{-1}), C=C aromatic rings (1606 and 1580 cm–^{1}), –NO (1517 cm^{-1}), and $–SO_2$ bonds (1606, 1580, 1517, 1344, 1235, and 1133 cm^{-1}), which were also observed for the free Vtx drug.[43] The findings suggest that ND_{Vtx} is largely composed of the free drug Vtx. To assess the various possible chemical and structural species within ND_{Vtx}, high- resolution tandem liquid chromatography/mass spectrometry (LC/MS) was performed. The LC chromatogram of sonicated Vtx identified 2 peaks (Figure 2a) eluted during analysis. The most predominant (high intensity) peak at 21.5 min, which is characteristic of free Vtx, decreased with increasing sonication time. Conversely, a new small peak appeared in the range of 19.5–20.5 min, which increased with sonication time. The corresponding electron spray ionization–mass spectrometry (ESI–MS) analysis of these LC peaks (Figure 2b(i), (ii)) showed

dominant mass-to-charge ratios (*m*/*z*) representing Vtx (868 *m*/*z*) at 21.5 min, and hydroxylated fragments (435 *m*/*z*) and dimers (1351 and 1750 *m*/*z*) at 20 min. Overall, from the LC/MS analysis, the possible chemical modifications that Vtx undergoes during sonication can be inferred and are represented in Figure 2c. The hydroxylated and dimerized species were present in low intensities (0.05% of total peak area at 320 nm) in comparison to the free drug, as noted in their representative LC peak area. We speculate that Vtx and the modified species can form oligomers on the reactive bubble surface that can facilitate the self-assembly of ND_{Vtx}.[38]

To determine the main interactive forces holding the NDs together, their disassembly profiles (Figure 2d,e) were studied under a range of conditions. ND_{Vtx} were incubated in urea, Tween 20, sodium chloride (NaCl), DMSO, ethylenediaminetetraacetic acid (EDTA), 2-(*N*-morpholino)ethanesulfonic acid (MES), and 3-(*N*-morpholino)propanesulfonic acid (MOPS) buffer, and the release of Vtx, which is an indication of ND_{Vtx} disassembly, was measured as a function of time (Figure 2e). A rapid release of Vtx was observed in Tween 20 and DMSO within 30 min (76%), as determined from UV–vis spectroscopy measurements of the supernatant (at 320 nm). However, a Vtx release of <25% even after 24 h was observed in urea (which corresponds to the rupture of H bonds), and in buffers that disrupt ionic interactions [NaCl, MES buffer (pH 3) and MOPs buffer (pH 7)]. This indicates that the dominant interactions holding the NDs together are hydrophobic in nature. Thus, the presence of aromatic rings in Vtx plays an important role in facilitating their sound-driven assembly into ND_{Vtx} through hydrophobic interactions upon bubble collapse.

Biological Activity of ND_{Vtx}. The release of Vtx from ND_{Vtx} was assessed in a range of biological media. ND_{Vtx} were suspended in 100% fetal bovine serum (FBS), McCoy complete media (with 10% FBS and 1% penicillin/streptavidin), and phosphate-buffered saline (PBS, pH 7)

at room temperature for up to 13 days. Post incubation, the NDs were centrifuged, and the absorbance of the supernatant was measured at 320 nm by UV–visible spectroscopy. As observed from Figure 3a(i), ~40% of the free drug was released cumulatively by day 13 in 100% FBS and McCoy complete media. The differing morphology of ND_{Vtx} before and after incubation in 100% FBS on day 13 (Figure 3a(ii)) confirmed the time-dependent disassembly of the NDs, leading to the release of the drug. A percentage release of only 18% was detected in PBS. In PBS and water, this release was accompanied with a small (~30%) decrease in average particle diameter over time (12 days) (from 248 to 178 nm in PBS) (Figure S1a). These results indicate the stability of the NDs in PBS and in water over time, with no obvious agglomeration observed within the 12-day incubation period examined, as suggested by the polydispersity index of the size distribution (Figure S1b). The slow release or disassembly of NDs in PBS or water could benefit storage, at least in the short term, such that drug release would predominantly occur in biological media where they are needed.

Vtx triggers cell death by binding to Bcl2 receptors in the mitochondria, which results in the release of the pro-apoptotic BH3 protein and activation of apoptosis. Thus, we examined the biological functionality of ND_{Vtx} using an Annexin V apoptotic assay coupled with propidium iodide (PI). A variety of cell lines, including Jurkat (T cells), HEK 293T, and MDA-MB-231 cells, were exposed to increasing doses of ND_{Vtx} and the free drug Vtx (0–50 μM). Fluorescein isothiocyanate (FITC)-labeled Annexin V identifies apoptotic cells (green), whereas PI binds to the DNA of dead cells (red), thus enabling the quantification of live cells (Annexin V^-/PI^-), early apoptotic cells (Annexin V^+/PI^-), late apoptotic cells (Annexin V^+/PI^+), and dead cells (Annexin V^-/PI^+) using flow cytometry (Figure 3b and Figure S2). As shown in Figure 3b, treatment with ND_{Vtx} or the soluble free drug resulted in similar proportions of apoptotic cells (sum of cells at

early and late apoptotic stages), which increased with increasing concentrations of ND_{Vtx} or Vtx. This finding was supported by confocal microscopy imaging (Figure 3c), which showed increasing late apoptotic cell population (as indicated by the yellow signal resulting from the colocalization of green and red signals in the same cell) with increasing concentration of ND_{Vtx}. These results show that the sonosynthesis of Vtx into ND_{Vtx} does not impair the biological activity of the drug.

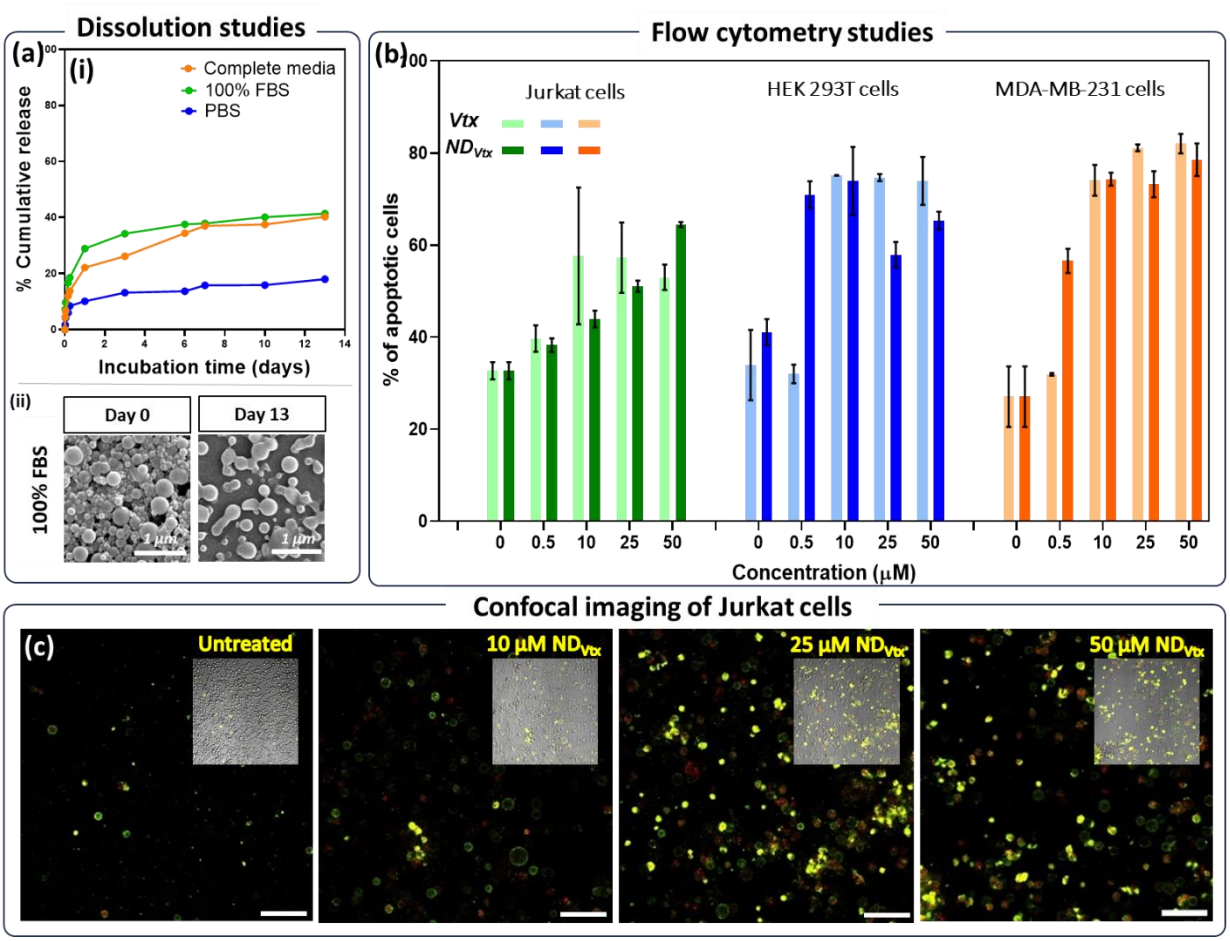

Figure 3. *In vitro* biological activity of ND_{Vtx}. (a) ND_{Vtx} dissolution in different biological media, as assessed by the (i) cumulative release of Vtx (absorbance readings at 320 nm) and (ii) SEM analysis of ND_{Vtx} at days 0 and 13 post incubation in 100% FBS. (b) Flow cytometry analysis of Jurkat, 293T, and MDA-MB-231 cells treated with increasing concentrations of ND_{Vtx} or free Vtx and assayed for apoptosis using Annexin V/PI staining. Data represent mean ± standard deviation

of three independent experiments (c) Confocal images of Jurkat cells treated with 0, 10, 25, or 50 μM ND_{Vtx} stained with Annexin V (green) and PI (red). The yellow signal results from colocalization of the green and red signals. Scale bars 20 μm.

Sonosynthesis and Characterization of Coassembled NDs. Vtx, as a mono therapeutic agent, is limited by its single therapeutic mechanism that cells can evade by developing resistance. Combining Vtx with other drugs that have synergistic modes of action can address this challenge.[6] Herein, we combined Vtx with Dox (an anthracycline drug) or S63845 (a Mcl1 inhibitor) to form coassembled $ND_{Vtx+Dox}$ and $ND_{Vtx+Mcl1}$, respectively (Figure 4a). Mono-assembled ND_{Dox} and ND_{Mcl1} were also prepared. The NDs had a nonhomogenous size distribution with average diameters of 300, 235, 275, and 409 nm for ND_{Mcl1}, $ND_{Vtx+Mcl1}$, ND_{Dox}, and $ND_{Vtx+Dox}$ respectively (Figure 4b) and ζ-potentials of –31, 0, –12, and 0 mV, respectively (Figure 4c). The negative charge is likely due to the hydroxylation of Dox and Mcl1 during sonication. All NDs, including the coassembled NDs, displayed a spherical morphology (Figure 4d). The chemical composition of the NDs post sonication was examined using high-performance liquid chromatography (HPLC). HPLC analysis of the disassembled ND_{Dox} and ND_{Mcl1} (Figure S3a,b) showed several peaks, indicating the presence of multiple modified species. $ND_{Vtx+Dox}$ and $ND_{Vtx+Mcl1}$ respectively showed characteristic peaks of Dox (10.5 min) and Mcl1 (16.2 min) alongside a Vtx peak (19 min) (Figure S3c,d). The chromatograms also revealed the elution of compounds other than the free drugs. However, the intensity of the peaks corresponding to these compounds represented only 3.3% of the total peak area at 320 nm. Further investigation of the chemical composition of $ND_{Vtx+Dox}$ using LC/MS showed two distinct peaks at 12.8 and 20.9 min (Figure S4a) on the LC chromatogram that corresponded to free Dox (489 *m*/*z*) and Vtx (868 *m*/*z*), respectively, on the MS patterns (Figure S4b,c). The LC pattern also displayed low intensity peaks between 14 and 18 min,

corresponding to a species with a *m*/*z* of 1254 (Figure S4d), which was likely an intermediate species chemically combining Dox and Vtx.

Overall, LC/MS analysis confirmed the presence of two drugs. The majority of both drugs in the formulations have retention times and molecular weights consistent with the free drugs, suggesting that their chemical structures are largely retained upon subject to high-frequency ultrasound treatment.

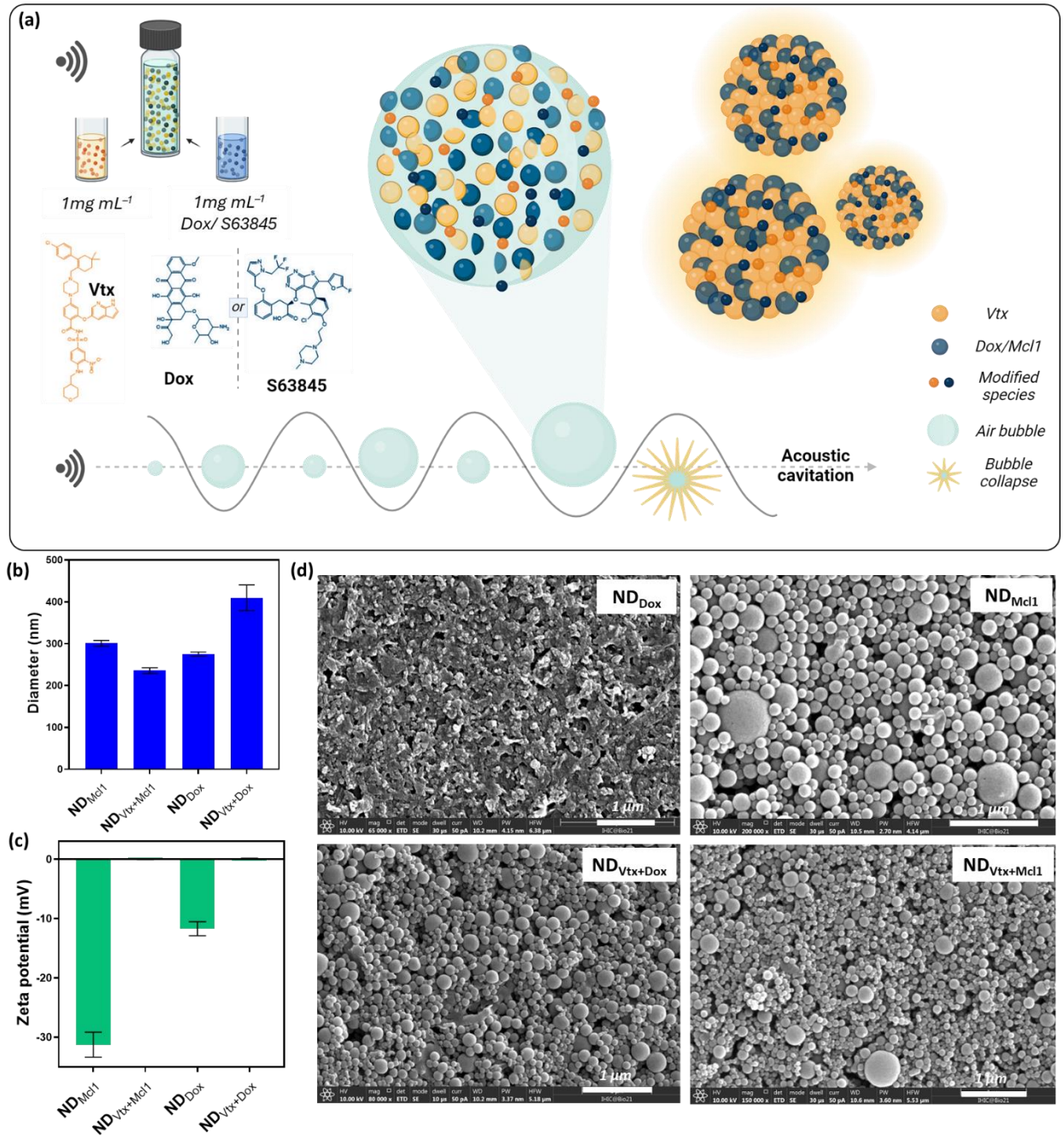

Figure 4. Coassembled NDs consisting of Vtx and either Dox or Mcl1 inhibitor (S63845). (a) Schematic representation of the self-assembly of more than one small molecule to form coassembled NDs. Characterization of the (b) particle diameter (measured by DLS in Milli-Q water) and (c) ζ-potential of mono- and coassembled NDs measured from three independent

experiments. Data represent averages ± standard deviations. (d) SEM images of the morphology of mono- and coassembled NDs. Figure 4a was created with BioRender.com.

The effects of changing the drug mass ratio on ND diameter, ζ-potential, and morphology were also studied by SEM and dynamic light scattering (DLS). Increasing the mass ratio of Vtx:Dox from 1:1 to 1:10 in the formulation resulted in a reduction of 16% in the average diameter of $ND_{Vtx+Dox}$ (Figure S5a) and a switch in the ζ-potential from neutral to negative of the coassembled ND (Figure S5b). In contrast, increasing the mass ratio of Vtx in the combination had little effect on the ND size (ranging between 530 to 1180 nm) and the ζ-potential remained neutral (Figure S5c,d). Note that ND_{Vtx} also had a neutral ζ-potential (Figure S5d). The neutral surface charge can be attributed to the low chemical modification in Vtx free drug during sonication. SEM images revealed that the coassembled NDs remained spherical upon changing the mass ratio (Figure S5e). HPLC analysis of the coassembled $ND_{Vtx+Dox}$ with varying masses indicated that more than 40% of the initial drug/s was assembled into the NDs (Figure S5f,g). For the subsequent studies, NDs coassembled at a mass ratio of Vtx and Dox/Mcl1 of 1:1 was used.

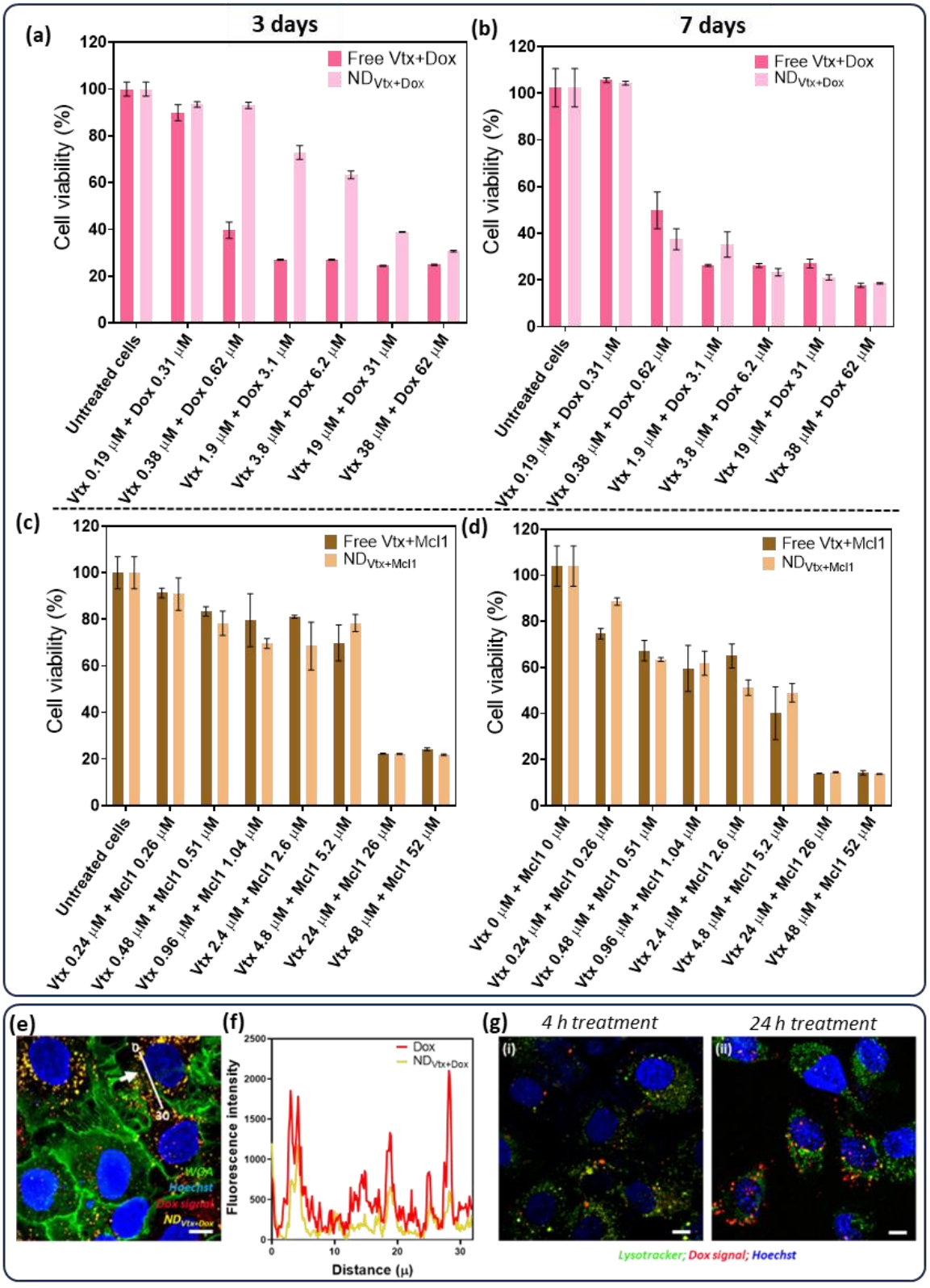

Figure 5. *In vitro* activity of coassembled NDs. Cytotoxicity profiles of (a,b) $ND_{Vtx+Dox}$ and (c,d) $ND_{Vtx+Mcl1}$ in SKOV-3 cells after 3 and 7 days of incubation. The free drug combinations at the

same mass ratios (Vtx:Dox/Mcl1 = 1:1) were used for comparison. Data in (a)–(d) represent mean ± standard deviation of three independent experiments (e) Representative confocal image of SKOV-3 cells treated with AF633-labeled $ND_{Vtx+Dox}$. Nuclei and cell membranes are stained with Hoechst (blue) and wheat germ agglutinin (WGA) (green), respectively. (f) Corresponding AF633-labeled $ND_{Vtx+Dox}$ and Dox signal distribution plots, for the region highlighted in white in (e). (g) Representative confocal images of SKOV-3 cells treated with 5 μM $ND_{Vtx+Dox}$ for (i) 4 or (ii) 24 h, stained with Lysotracker Green DND26 (green) and Hoechst (blue). The inherent Dox signal from the ND is shown in red. Scale bars 2.5 μM.

***In Vitro* Assessment of Mono- and Coassembled NDs.** As combination therapy is used as a strategy to address drug resistance, we studied the *in vitro* activity of the coassembled NDs using the cancer cell line SKOV-3, which is known to be resistant to various chemotherapeutic drugs, including Dox, Vtx, and paclitaxel.[9,44] The cytotoxicity of $ND_{Vtx+Dox}$ and $ND_{Vtx+Mcl1}$ (containing Vtx and Dox/Mcl1 at a mass ratio of 1:1) was evaluated and compared. Controls with free drug mixtures at comparable concentrations were used. The half-maximal inhibitory concentration (IC_{50}) of $ND_{Vtx+Dox}$ (which is defined as the drug concentration required to kill 50% of the cells) after 3 days of incubation was observed to be between Vtx 3.8 μM + Dox 6.2 μM to Vtx 19 μM + Dox 31 μM. In contrast, the IC_{50} of the free drug was at Vtx 0.38 μM + Dox 0.62 μM (Figure 5a). For longer exposures, *i.e.*,7 days treatment, the IC_{50} of $ND_{Vtx+Dox}$ decreased to Vtx 0.38 μM + Dox 0.62 μM, which was comparable to that of the free drug (Figure 5b). This could be attributed to the time-dependent dissolution of the coassembled NDs (Figure S6a) in cell culture media. In addition, the toxicity of $ND_{Vtx+Mcl1}$ showed an IC_{50} between Vtx 4.8 μM + Mcl1 5.2 μM to Vtx 24 μM + Mcl1 26 μM and Vtx 2.4 μM + Mcl1 2.6 μM after 3 and 7 days of treatment, respectively (Figure 5c,d). Both the $ND_{Vtx+Mcl1}$ and the mixed free drug showed comparable viability profiles.

In general, the coassembled NDs containing Vtx and Dox showed higher cytotoxicity than either free Vtx or ND_{Vtx} as mono-therapeutic agents against Vtx-resistant SKOV-3 (Figure S6b,c). This could be attributed to the synergistic action of Dox and Vtx.[10] To highlight the improved therapeutic capacity of the coassembled $ND_{Vtx+Dox}$, an additional control experiment using a combinatorial treatment of mono-assembled ND_{Vtx} and mono-assembled ND_{Dox} was performed. The cytotoxicity of free Vtx+Dox individually loaded ND_{Vtx}+ND_{Dox}, and coassembled $ND_{Vtx+Dox}$ was evaluated after 7 days of treatment (Figure S6c). The IC_{50} of the coassembled $ND_{Vtx+Dox}$ and free Vtx+Dox was observed between Vtx 0.19 µM + Dox 0.31 µM and Vtx 0.38 µM + Dox 0.62 µM, and Vtx 0.38 µM + Dox 0.62 µM respectively. However, the individually loaded ND_{Vtx}+ND_{Dox} only showed ~10 to 20% toxicity between Vtx 0.76 µM + Dox 1.24 µM and Vtx 0.38 µM + Dox 0.62 µM and did not reach 50% even at Vtx 38 µM + Dox 62 µM. The toxicity of the coassembled $ND_{Vtx+Dox}$ can be attributed to the combination of Dox + Vtx as a single particle and their low sono-chemical modification (Figure S3a,c). In particular, the activity of Dox appears to influence the synergistic behavior and hence the toxicity of the coassembled $ND_{Vtx+Dox}$. The chemical modification (*i.e.*, fragmentation and dimerization) of Dox within ND_{Dox} (Figure S3a) likely decreased its efficacy, which is consistent with our previous study on the sonoresponsiveness of Dox.[25] In the case of the coassembled system ($ND_{Vtx+Dox}$), the structure of Dox was more preserved when synthesized in combination with Vtx, as seen in Figure S3c. The minimal modification in Dox makes $ND_{Vtx+Dox}$ more active than the mono-component ND_{Dox} system, promoting better synergistic activity with Vtx. This is also supported by the similar toxicity observed for $ND_{Vtx+Dox}$ and the free Vtx+Dox mixture at day 7 *in vitro* (Figure 5b). We speculate that the sonochemically modified Vtx acts as an excipient that can trap free Dox and free Vtx in their unmodified forms within a nanoparticle formulation, as suggested by our HPLC and

LC/MS data (Figures S3 and S4). Drug (Vtx) release from $ND_{Vtx+Dox}$ or ND_{Vtx} followed a similar trend (Figure 3a, Figure S6a), suggesting that ND disassembly from the coassembled or mono-component NDs is similar and unlikely to influence the synergistic behavior of $ND_{Vtx+Dox}$.

Confocal microscopy was used to investigate the internalization of Alexa Fluor (AF)633-labeled $ND_{Vtx+Dox}$ by SKOV-3 cells (Figure 5e). Cytoplasmic localization of AF633-labeled $ND_{Vtx+Dox}$ was observed, which colocalized with the Dox signal (Figure 5f). Lysotracker staining was used to study the intracellular trafficking of the coassembled NDs. The colocalization of ND (red) with lysosomes (green) after 4 h incubation of SKOV-3 cells with AF633-labeled NDs is shown in Figure 5g(i) and was estimated by a Pearson correlation curve (Figure S7c(i)). High colocalization of the NDs with lysosomes was observed at 4 h, whereas at 24 h, the Pearson's correlation scatter plot suggests lower colocalization of NDs and lysosomes (Figure S7c(ii)), potentially through endosomal escape of NDs in the cytosol. In addition, the mean fluorescence intensity of the NDs per cell in confocal images increased with incubation time (from 4 to 24 h), indicating higher uptake of the NDs over time (Figure S7d). Overall, these imaging studies suggest that $ND_{Vtx+Dox}$ are internalized in cells, then localize in the endo-lysosomal compartments in the first 4 h, and eventually escape by 24 h at 37 °C.

***In Vivo* Biodistribution and Tumorigenicity of ND_{Vtx}, ND_{Dox}, and $ND_{Vtx+Dox}$.** *In vivo* studies for assessing the biodistribution and tumor reduction capacity of the NDs were performed on 6-week-old female BALB/c nu/nu mice (Figure 6a). The animal tumor model was obtained by injecting luciferase-expressing SKOV-3 cells (SKOV-3 luc) subcutaneously in the flank of mice. Tumor growth and body weight were monitored from the day of injection (day 0) until the tumors reached 20–50 mm^3 in volume (day 39). Post establishment of tumors, the mice were randomized into 6 treatment groups: ND_{Vtx}, ND_{Dox}, $ND_{Vtx+Dox}$, free Vtx, free Dox (all at 2 mg kg^{-1}), and a PBS

control group. All NDs were labeled with rhodamine 800 (Rh800). The treatments were administered *via* intravenous (IV) injection (in the tail vein) on day 39. The IV injection for the treatment was then repeated for a total of 6 injections within 3 weeks (Figure 6a). The mice were monitored daily for weight and body score, and tumor progression (tumor size) was assessed twice a week. Animals were sacrificed once the tumor mass reached >5% of their body weight or post 6 drug injections (experimental end point).

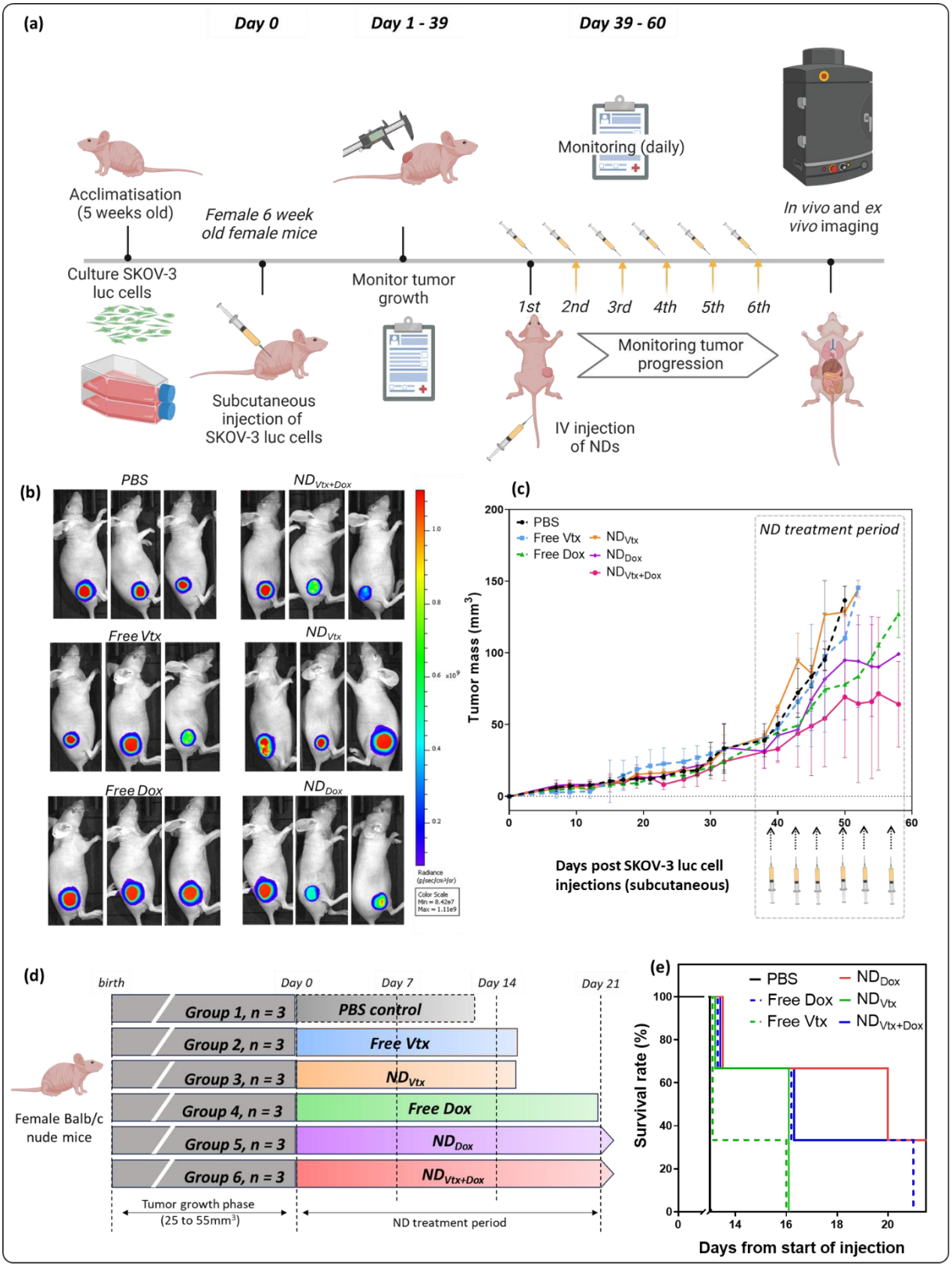
(a)
Day 0
Day 1 - 39
Day 39 - 60
Acclimatisation (5 weeks old)
Culture SKOV-3 luc cells
Female 6 week old female mice
Subcutaneous injection of SKOV-3 luc cells
Monitor tumor growth
Monitoring (daily)
1st
2nd
3rd
4th
5th
6th
Monitoring tumor progression
IV injection of NDs
In vivo and ex vivo imaging
(b)
PBS
ND Vtx+Dox
Free Vtx
ND Vtx
Free Dox
ND Dox
(c)
PBS
Free Vtx
Free Dox
ND Vtx
ND Dox
ND Vtx+Dox
ND treatment period
Tumor mass (mm3)
Days post SKOV-3 luc cell injections (subcutaneous)
(d)
birth
Day 0
Day 7
Day 14
Day 21
Group 1, n = 3
PBS control
Group 2, n = 3
Free Vtx
Group 3, n = 3
ND Vtx
Group 4, n = 3
Free Dox
Group 5, n = 3
ND Dox
Group 6, n = 3
ND Vtx+Dox
Female Balb/c nude mice
Tumor growth phase (25 to 55mm3)
ND treatment period
(e)
PBS
Free Dox
Free Vtx
ND Dox
ND Vtx
ND Vtx+Dox
Survival rate (%)
Days from start of injection

Figure 6. *In vivo* tumor inhibition studies. (a) Experimental design of tumor localization and reduction in Balb/c nu/nu (nude) mice after six consecutive IV ND injections within 3 weeks. (b) Bioluminescence IVIS imaging of the tumor (SKOV-3 luc)-bearing mice, grouped by treatment type, and imaged at their endpoint. (c) Tumor growth curves represented as tumor mass (mm^3) from day 0 to day 59. (d) Schematic overview of the different treatment groups and their survival profiles. (e) Survival curves of the different treatment groups during the treatment period. Figure 6a and 6d was created with BioRender.com.

Luminescence imaging of the tumors using an In Vivo Imaging System (IVIS) revealed that the ND_{Dox} and $ND_{Vtx+Dox}$ treatment groups had relatively smaller tumors at the endpoint in comparison to the free Dox, free Vtx, ND_{Vtx} and PBS control groups (Figure 6b). Tumor growth curves (Figure 6c) support these results, where a slower tumor growth was observed for tumors treated with ND_{Dox} or $ND_{Vtx+Dox}$ in comparison to that observed for the other groups. In terms of survival rate, as expected, the PBS control group showed the shortest survival among all groups, as the tumor volumes reached the end point faster (13 days) in the absence of treatment (Figure 6d). The free Vtx- and ND_{Vtx}-treated groups survived up to 16 days post treatment (Figure 6e). This confirms the lower efficacy of mono-therapeutic Vtx (as both free and ND formulation) on resistant SKOV-3 cells. Free Dox slowed tumor progression in comparison to the PBS control and improved the life span of the mice by 21 days (Figure 6e). Animals treated with ND_{Dox} (1 out of 3 mice) and $ND_{Vtx+Dox}$ (1 out 3 mice) survived to day 22 and longer (Figure 6e) *i.e.*, the tumor mass measured at the experimental endpoint was still <5% of mice body weight. However, the animals were sacrificed due to a defined experimental endpoint (post 6 injections). Overall, ND_{Dox} and $ND_{Vtx+Dox}$ improved the lifespan of tumor-bearing mice by at least 6 days (~24%) in comparison to free Vtx or ND_{Vtx} and at least 10 days (~40%) in comparison to the PBS control. The tumor inhibition

activity of the NDs on SKOV-3 luc-induced tumor highlights the effectiveness of the NDs against drug-resistant cancer models.

The *in vivo* and *ex vivo* biodistribution of Rh800-labeled NDs, *i.e.*, ND_{Vtx}, ND_{Dox}, and $ND_{Vtx+Dox}$, were also studied by IVIS imaging after the 3rd and 6th injections. *In vivo* imaging of the whole animal showed no significant fluorescence signals in the dorsal (posterior), ventral (anterior), or distal (right) regions. However, the proximal (left) regions showed some fluorescence after the 3rd injection but diminished after the 6th injection in the case of ND_{Dox} and $ND_{Vtx+Dox}$ (Figure S8). Major organs, including tumor, heart, kidney, spleen, lung, liver, and brain, were therefore harvested and imaged *ex vivo*. After the 3rd injection, the Rh800 signal was highly localized in the kidney, tumor, and lung (Figure 7a). In addition, a weaker signal was seen in the heart and the spleen. Post 6th injection, a high signal was observed in the kidneys and a weaker signal in the tumor, heart, and spleen (Figure 7b). We note that the signal from the lung was cleared by the end of the treatment period. To confirm that the signal was not due to free dye, we studied the biodistribution of free Rh800 dye *in vivo*. Imaging showed the accumulation of the free dye in the kidney at 0.25, 0.5, 1, and 4 h, which reduced by 50% by 24 h (Figure S9). The presence of free dye in the kidney could mean that the free dye dissociates from the NDs as the nanoaggregates disassemble and accumulate in the kidney for clearance. However, a signal in other organs, including the tumor, is likely from ND accumulation rather than the free dye.

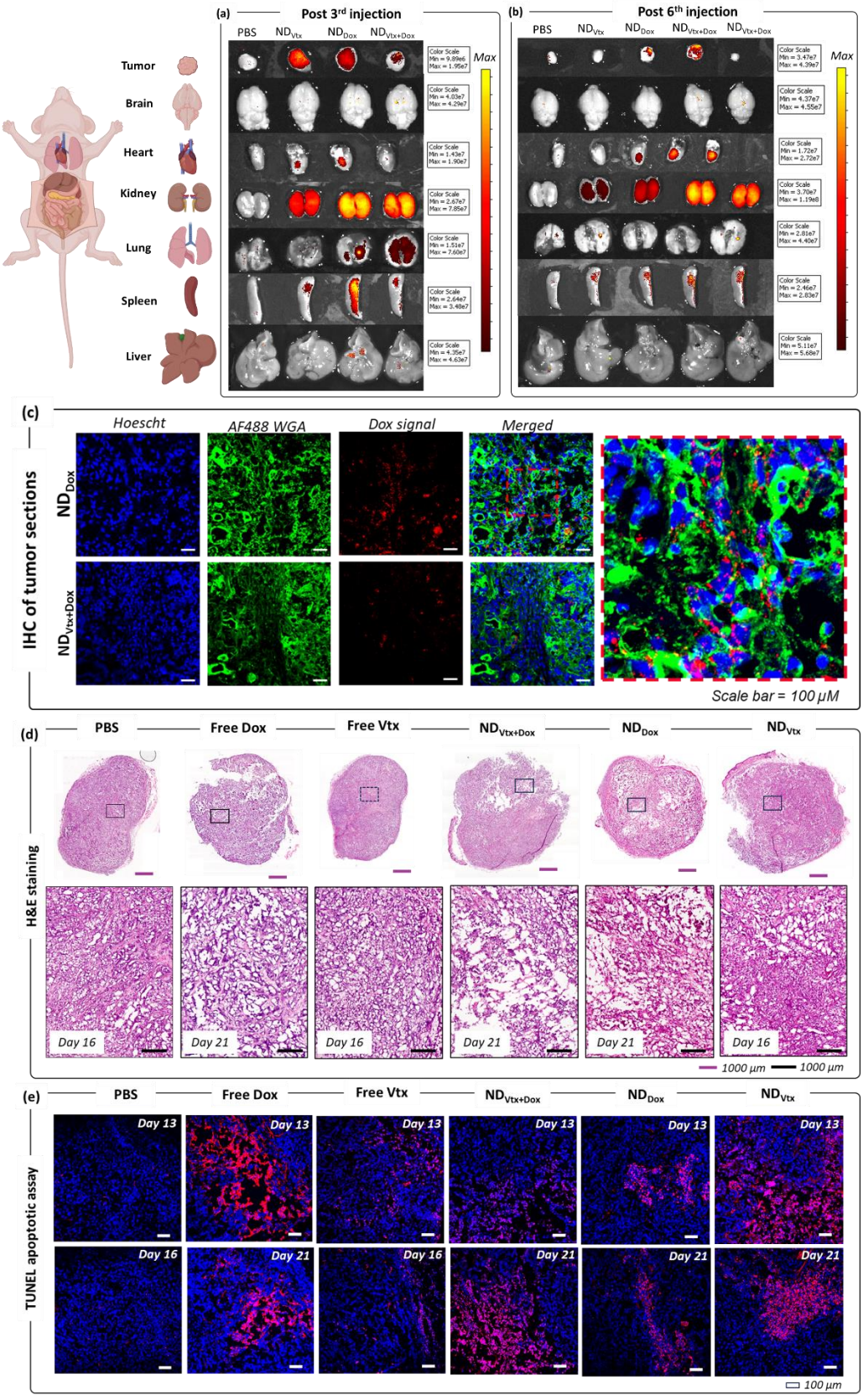
(a)
Post 3rd injection
PBS
NDVtx
NDDox
NDVtx+Dox
Max
(b)
Post 6th injection
PBS
NDVtx
NDDox
NDVtx+Dox
NDVtx+Dox
Max
Tumor
Brain
Heart
Kidney
Lung
Spleen
Liver
(c)
Hoescht
AF488 WGA
Dox signal
Merged
IHC of tumor sections
NDDox
NDVtx+Dox
Scale bar = 100 μM
(d)
PBS
Free Dox
Free Vtx
NDVtx+Dox
NDDox
NDVtx
H&E staining
Day 16
Day 21
Day 16
Day 21
Day 21
Day 16
1000 μm
1000 μm
(e)
PBS
Free Dox
Free Vtx
NDVtx+Dox
NDDox
NDVtx
TUNEL apoptotic assay
Day 13
Day 16
Day 21
100 μm

Figure 7. *In vivo* biodistribution and tumor accumulation of the NDs. *Ex vivo* IVIS fluorescence imaging of mice organs treated with Rh800-labeled ND_{Vtx}, ND_{Dox}, or $ND_{Vtx+Dox}$ at (a) 4 h and (b) 24 h post IV injection. (c) Representative immunohistochemistry images of tumor tissues collected from ND_{Dox} and $ND_{Vtx+Dox}$ on day 21 showing stained nucleus (blue), cell membrane (green) and inherent nanoparticle signal (red). IHC, Immunohistochemistry. (d) H&E staining of tumor sections collected from different treatment groups, at the experimental end point on either day 16 or 21. (e) Representative confocal images of tumor tissues on which a TUNEL apoptotic assay was performed. The tissues are stained with Hoechst (blue) and TUNEL to label fragmented DNA (red). The colocalization (pink) of blue and red signals indicates apoptotic cells. The schematics in Figure 7a and 7b were created with BioRender.com.

To confirm the accumulation of the NDs and their therapeutic effect, histology of the harvested organs was performed followed by confocal microscopy. The ND_{Dox}- and $ND_{Vtx+Dox}$-treated tumors showed a distinct red signal emitted by Dox on day 21, confirming tumor deposition (Figure 7c). No Dox signal was observed in the free Dox-treated tumor sections, which was likely due to the rapid clearance of the free drug (Figure S10). The colocalization of signals from Dox and Rh800 (ND labeling) in the ND_{Dox}- and $ND_{Vtx+Dox}$-treated tumors emphasizes the presence of NDs within the tumor (Figure S11).

Hematoxylin & eosin (H&E) staining was performed to observe the morphology of the tumor tissue (Figure 7d). Mice treated with free Vtx or ND_{Vtx} showed tumor morphology similar to the control PBS group, which confirms their low activity at the tumor site. In contrast, tumors treated with free Dox, ND_{Dox}, or $ND_{Vtx+Dox}$ showed tissue damage at day 13 (Figure S12a), which became more pronounced at day 21 (Figure 7d). Tissue damage was further confirmed using terminal deoxynucleotidyl transferase dUTP nick end labeling (TUNEL) staining. The TUNEL assay labels

3′-OH ends of fragmented DNA, which is a hallmark of apoptosis in cells. The colocalization of the signal from fragmented DNA (red) and the nucleus stained with Hoechst (blue) into a pink/violet signal indicates signs of apoptosis in the tumor tissues (Figure 7e). In general, a longer treatment (21 days *vs* 13 days) resulted in increased TUNEL signal, suggesting higher apoptosis caused by multidose injections. Free Vtx-treated tumors showed the lowest apoptosis signals on day 21 among all treatment groups, providing further evidence of the resistance of SKOV-3 cells to Vtx. ND_{Vtx} showed enhanced apoptotic signals in comparison to the free Vtx, highlighting their potential in combating drug resistance in SKOV-3 cell lines. However, future dosage and treatment duration optimization studies are required to confirm this. Overall, increased apoptosis was observed in tumors treated with free Dox, ND_{Dox}, or $ND_{Vtx+Dox}$ than tumors treated with PBS, which was consistent with the tissue damage observed in the H&E staining analysis. Thus, our findings suggest that the NDs accumulate in the tumors and control the progression of tumor growth through cell apoptosis.

To investigate the safety of the NDs and eliminate possible nonspecific tissue toxicity, major organs, such as lung, heart, liver, kidney, brain and spleen, were harvested and stained with H&E and evaluated by histology (Figure S13). Overall, mice treated with ND_{Vtx}, ND_{Dox}, or $ND_{Vtx+Dox}$ showed no significant morphological differences or tissue damage in major organs compared to the PBS control group. We note that ND_{Dox} and $ND_{Vtx+Dox}$ accumulation in the lung post 3rd injection do not cause obvious toxicity in the lung tissues as they were cleared at the experiment end point (6th injection). These studies suggest that transforming small anticancer molecules into NDs using high-frequency ultrasound can pave the way for improved tumor treatments while potentially reducing nonspecific toxicity. It has been demonstrated that leaky blood vessels and poor lymphatic drainage in the tumor microenvironment can facilitate the deposition and retention

of nanoparticles in tumor tissues.[45] It is likely that transforming small molecules into NDs can promote their retention in tumor tissues, resulting in the sustained release of drug over time.

CONCLUSION

The high-frequency ultrasound-driven synthesis of carrier-free particles composed of one (Vtx) or two anticancer drugs (Vtx and Dox or S63845) was reported. The synthesized NDs combine the advantages of nanosized drug delivery systems (in aqueous solutions) without the use of additional carriers or organic solvents. The ND_{Vtx} were stable in serum and retained their apoptotic activity post sonosynthesis. The coassembled systems, $ND_{Vtx+Dox}$ and $ND_{Vtx+Mcl1}$, showed cytotoxic activity in a partially resistant cell line SKOV-3, which was comparable to the free drug after 7 days of incubation. The *in vivo* activity of the NDs studied in a xenograft tumor mouse model showed that $ND_{Vtx+Dox}$ treatment reduced tumor growth most efficiently after 21 days of treatment and improved the survival rate of the mice by at least 40% (10 days). *Ex vivo* imaging of the mice tissues treated with fluorescently labeled NDs showed accumulation of the NDs in the tumor post 3^{rd} and 6^{th} injections, which was confirmed by histology and an apoptosis assay. The NDs did not cause significant tissue damage in other organs, including the lung, kidney, spleen, liver, brain, and heart. Carrier-free NDs can therefore serve as effective chemotherapeutic platforms for *in vivo* delivery of combination therapies. The versatility of the nanodrug assembly technique can be applied to other aromatic drugs to modulate pharmacokinetics for the potential treatment of diverse diseases or other small molecules for biosensing applications.

EXPERIMENTAL SECTION

Materials. Vtx and S63845 (Mcl1 inhibitor) were purchased from Selleck Chemicals. Doxorubicin hydrochloride, acetonitrile (suitable for HPLC, ≥99.9%), urea, Tween 20, NaCl, DMSO, EDTA, MES, MOPS, bovine serum albumin (BSA), and xylenes (histological grade) were

purchased from Sigma Aldrich. Formic acid (98–100%) was purchased from Thermo Fisher Scientific. Hoechst 33342 trihydrochloride salt (10 mg mL^{-1}), AF488-WGA, Annexin V, AF488 conjugate for apoptosis detection coupled with PI, 2,3-bis-(2-methoxy-4-nitro-5-sulfophenyl)-2*H*-tetrazolium-5-carboxanilide) (XTT) cell viability assay, Dulbecco's modified Eagle medium (DMEM), Roswell Park Memorial Institute (RPMI), McCoy's 5A (modified) medium, and PBS were purchased from Life Technologies. Rhodamine 6G and Rh800 dyes were purchased from Sigma Aldrich. AF633 NHS ester, Lysotracker Green DND26, collagen I recombinant rabbit monoclonal primary antibody, goat anti rabbit IgG (H+L) cross-absorbed secondary antibody (AF488), and SlowFade diamond antifade mountant were purchased from Invitrogen. R&D Systems Cultrex PathClear basement extract (5 mL) was purchased from In Vitro Technologies. Triton X 100LR (Teric X10) was purchased from CSA Scientific, ChemSupply Australia. Peroxidase-Anti-Peroxidase Pen liquid blocker was purchased from Newcomer Supply Laboratory. H&E staining for histology was purchased from MedChemExpress. Superfrost Plus adhesion glass slides (RNAse free) were purchased from ProSciTech. Water with a resistivity greater than 18.2 MΩ cm (Milli-Q water) was obtained from a three-stage Millipore Milli-Q plus 185 purification system (Millipore Corporation, USA). All aqueous solutions were filtered through 220 nm diameter membranes before use in cell and animal experiments.

Synthesis of NDs. Vtx (or Dox) was dissolved in water (500 μL) at a concentration of 1 mg mL^{-1} and sonicated at 3.2, 5.6, or 8 W cm^{-2} using an ELAC Nautik generator paired to an ultrasound transducer (T&C Power Conversion, Inc.) vibrating at a frequency of 490 kHz for 60 min. The nanoaggregates formed post sonication were purified by centrifuging at 9000*g* for 10 min followed by three washing cycles in Milli-Q water (1000*g*, 10 min). Finally, the ND pellets were dispersed

in Milli-Q water and stored at room temperature. Vortexing was performed prior to each wash cycle to thoroughly disperse the pellets.

To synthesize coassembled NDs (*i.e.*, $ND_{Vtx+Dox}$ and $ND_{Vtx+Mcl1}$), drugs were dissolved in water (500 μL) to reach a final concentration of 1 mg mL^{-1} and sonicated at 490 kHz and 5.6 W cm^{-2} for 60 min. The nanoaggregates formed were purified as described above for single ND preparation.

To study the influence of drug concentration on the ND diameter and morphology, $ND_{Vtx+Dox}$ was prepared with different concentrations of Vtx (0.1, 0.2, 0.5, and 1 mg mL^{-1} in Milli-Q water (500 μL)), while the concentration of Dox remained constant at 1 mg mL^{-1}. NDs were also prepared with varying concentrations of Dox (0.1, 0.2, 0.5, and 1 mg mL^{-1} in Milli-Q water (500 μL)), while keeping the concentration of Vtx constant at 1 mg mL^{-1}. ND synthesis was performed at 490 kHz and 5.6 W cm^{-2} for 60 min and washed at 9000*g* for 10 min.

For all ND preparations, Vtx and Mcl1 inhibitor were prepared in DMSO, whereas Dox was prepared in Milli-Q water, at stock concentrations of 50 mg mL^{-1}. Further dilutions were performed in Milli-Q water before sonication.

ND Characterization. Particle size distributions were measured in Milli-Q water using DLS (Zetasizer Nano ZS, Malvern Instruments) and NTA on a Malvern NanoSight NS300 instrument (with a 405 nm laser and 65 mW output). Particle morphology was imaged using SEM. For SEM analysis, a small volume (~7 μL) of the synthesized NDs was placed onto a silicon wafer and dried in air at room temperature overnight. The dried samples were coated with a 5 nm gold turbo-pumped sputter coater (Quorum Q150T), followed by imaging on an FEI Teneo VolumeScope instrument at an operating voltage of 20 kV.

Characterization of ND Composition. UV–Visible absorption measurements were performed on 1 μM ND_{Vtx} disassembled in 10% DMSO and suspended in Milli-Q water, using a Specord 250

Plus UV–visible spectrophotometer (Analytik Jena, Jena, Germany). FTIR spectroscopy measurements were performed to identify the occurrence of hydroxylation in the NDs. The synthesized and disassembled (in 10% DMSO) ND_{Vtx} were freeze-dried (using a Heto Drywinner freezer dryer), and the powdered samples were analyzed using a Bruker TENSOR II FTIR instrument.

HPLC was performed to identify chemical changes and mass variations in Vtx post ND assembly. For HPLC analysis, NDs were disassembled in 10% DMSO and analyzed using a Shimadzu LC-20 AD Series HPLC instrument equipped with a UV detector connected to a Jupiter 5 μm C18 300, LC column 250 (column length) × 4.6 (internal diameter) mm. The samples were eluted at a constant flow rate of 1 mL min^{-1} and a temperature of 37 °C using acetonitrile and Milli-Q water containing 0.1% formic acid as elution buffers. An aliquot (100 μL) of NDs or sonication product was injected into the column using linearly increasing gradient of acetonitrile from 0 to 95% in 40 min, followed by a final 20-min wash in 95% water.

ESI–MS was performed using a single Quadrupole Mass Spectrometer coupled to the above HPLC instrument. MS was operated in positive ion mode at 40 °C.

ND Stability and Release *In Vitro*. ND_{Vtx} (2 μg mL^{-1}) were suspended in Milli-Q water, urea (100 mM), Tween 20 (100 mM), NaCl (100 mM), DMSO (100%), EDTA (100 mM), MES (pH 3, 100 mM), or MOPS (pH 8, 100 mM). The suspensions were pipetted into Slide-A-Lyzer MINI dialysis devices (molecular weight cutoff 2k) and placed in a 48-well plate containing Milli-Q water (500 μL) per well (reservoir). Free Vtx (molecular weight 868.4 g mol^{-1}) that released from the NDs diffused through the dialysis membrane and accumulated in the reservoir. The concentration of the free drug in the reservoir was determined by measuring the absorbance of the

supernatant at 320 nm for Vtx at different timepoints using a Specord 250 Plus UV–vis spectrophotometer.

The same procedure was used to measure drug release (from ND_{Vtx} and $ND_{Vtx+Dox}$) in complete DMEM media (with 10% FBS), 100% FBS, and PBS (pH 7) using a starting ND concentration of 3 μM. The released Vtx and Dox were determined *via* UV absorbance measurements at 320 nm and 476 nm (broad peak), respectively.

For the size stability studies, ND_{Vtx} was incubated in PBS and Milli-Q water for up to 12 days and their average diameter measured on day 0, 1, 5, 7, 8, 10, and 12 using DLS.

Cell Lines. MDA-MB-231, Jurkat, 293T, and SKOV-3 cells were purchased from the American Type Culture Collection. For the apoptotic studies, adherent MDA-MB-231 and 293 T cells were cultured in DMEM complete media and suspension Jurkat cells were cultured in RPMI complete media. For the cell viability studies, SKOV-3 cells were cultured in McCoy's 5A (modified) medium. The IVISbrite SKOV-3 Red F-luc bioluminescent tumor cell line (Bioware Brite) was purchased from Revvity and cultured in complete McCoy's 5A (modified) medium for *in vivo* studies. All complete media were supplemented with 10% FBS and 1% penicillin-streptomycin. All cells were cultured at 37 °C, 5% CO_2, and 95% humidity.

Cell Apoptosis. The apoptotic activity of the NDs was determined using an FITC-conjugated Annexin V coupled to PI assay (Invitrogen). MDA-MB-231, 293T, and Jurkat cells were seeded (60000 cells per well) on a 48-well plate. Cells were incubated with varying concentrations (0–50 μM) of free Vtx or ND_{Vtx} for 48 h. After incubation, the adherent cells (293T cells and MDA-MB-231) were trypsinized for 2 min and washed by centrifugation at 350*g* for 5 min. Annexin V-FITC (5 μL from stock) and PI (1μL of 100 μg mL^{-1}) were suspended in 1X annexin-binding buffer and added to each well (100 μL) and incubated for 15 min as per the manufacturer's protocol. Treated

samples were analyzed for Annexin V (green) and PI (red) fluorescence using a BD Accuri C6 Plus flow cytometer (BD Bioscience, San Jose, CA, USA) and a Nikon A1R+confocal laser scanning microscope (Nikon Corporation, Tokyo, Japan).

Cell Viability. SKOV-3 cells were seeded on a 96-well plate at a seeding density of 25000 cells per well overnight. Free Vtx+Dox, ND_{Vtx}+ND_{Dox} (NDs mixed at a ratio of 1:1), or $ND_{Vtx+Dox}$ (Vtx:Dox = 1:1 coassembled during sonication) were added at titrating concentrations of 0, 0.5, 1, 2, 5, 10, 50, and 100 μM. The cytotoxicity was tested *via* the XTT assay. XTT reagent (10.8 mg) was added to McCoy media (54 mL) then supplemented with *N*-methyl benzopyrazine sulphate (2 mM). Cells were treated with the NDs for 3 and 7 days, after which cells were washed with PBS and resuspended with activated XTT/*N*-methyl benzopyrazine sulphate reagent (300 μL) for 3 h. Absorbance was measured using an Infinity M200 Pro Tecan microplate reader. Untreated cells served a negative control.

Internalization and Localization. ND_{Vtx} and $ND_{Vtx+Dox}$ were labeled with Rhodamine 6G post sonication by incubating the NDs in the dye for 1 h at room temperature and subsequent washing for 3–5 times at 9000*g* for 10 min to remove excess dye. Labeling was confirmed by measuring the absorbance at 700 nm. SKOV-3 cells were seeded in an 8-well chamber at 60000 cells per well overnight. The labeled NDs were added to the cells at a concentration of 5 μM (300UL) and incubated for 48 h. Post incubation, the cells were washed in PBS, fixed in 4% paraformaldehyde for 10 min and imaged using a Nikon A1R+ confocal microscope.

To determine cellular localization, SKOV-3 cells were seeded (30000 cells per well) in an 8-well chamber and treated with $ND_{Vtx+Dox}$ (5 μM). After 72 h of incubation at 37 °C, the cells were washed with PBS (200 μL) and incubated with LysoTracker Green-DND26 (100 nM) for 1 h at 37 °C as per the manufacturer's protocol. Following incubation, the nuclei were stained with

Hoechst 33342 (0.07 μM, 300 μL per well) for 15 min, followed by washing in PBS to remove excess stain. The samples were imaged using a confocal laser scanning microscope using a 40× water objective and a 100× oil objective. All staining procedures were performed at room temperature.

Animal Models and Housing. All procedures were conducted in accordance with the Australian code for the care and use of animals for scientific purposes, and experiments were approved by the University of Melbourne Animal Ethics Committee (IDs. 10453 and 10404). Six weeks old immunocompromised nude mice on a BALB/c background (BALB/c-Foxn1nu/Arc) were purchased from the Animal Resources Centre (Western Australia) and transported to the Peter Doherty Bioresources Facility (Melbourne, Australia) using recognized transport courier. On arrival, the mice were maintained under barrier conditions for at least 7 days prior to commencing experiments. Mice were housed in groups of 4 mice per cage and on a 12 h light/dark cycle with *ad libitum* access to food and water.

***In Vivo* Antitumor Studies.** Firefly luciferase SKOV-3 cells (5×10^6) were suspended in 100 μL of complete cell culture media with basement membrane extracts (DMEM and cultrex respectively (1:1)). This mixture was subcutaneously injected (27G needle) into the flank of each mouse (6-week-old female) to induce a tumor xenograft model. The tumor growth was monitored thrice a week using calipers and the tumor mass was calculated using the formula: tumor mass (mm^3) = ($W^2 \times L$)/2) × 1.056, where L is the longest diameter (mm), W is the shortest diameter (mm), and the 1.056 g cm^{-1} is the density of connective tissues. Once the tumor mass reached 20–50 mm^3 (4 weeks; day 39) in size, the tumor-bearing mice were randomized into 6 groups. Post randomization, the mice were intravenously injected (30G needle) with 100 μL of PBS, free Dox, free Vtx, ND_{Dox}, ND_{Vtx}, or $ND_{Vtx+Dox}$ at a dose of 2 mg kg^{-1} per injection. Following the first

injection, the treatment groups were sequentially dosed with respective drugs twice a week for 3 weeks (6 total injections). After each IV injection, the mice were monitored daily, *i.e.*, the weight (g) and tumor mass (mm^3) were recorded twice a week. The mice were removed from the experiment at experimental end point and/or culled once the tumor size reached >5% of the mice body weight and/or the mice showed failure to maintain weight within 15% compared to standard weights for the age/sex/strain.

***In Vivo* Imaging.** Once the mice reached the experimental end point, *in vivo* whole animal and *ex vivo* organ imaging were performed using a Xenogen IVIS Lumina system (PerkinElmer) equipped with a Living Image software (version 4.5).

Bioluminescence Imaging. Bioluminescence imaging was performed by intraperitonially injecting 150 mg/kg D-luciferin (~100 μL in 20 g mice) in mice. Post 8–10 min injection, the mice were anesthetized and imaged for bioluminescence signals on the flank bearing the xenograft tumor induced by firefly luciferase-expressing SKOV-3 cells. All images were acquired under the same parameters: exposure time of 20 s, small binning factor, and field of view of 12.5 cm.

Fluorescence Imaging. ND_{Vtx}, ND_{Dox}, or $ND_{Vtx+Dox}$ injected into the mice were labeled with Rh800 dye (excitation/emission wavelengths = 682 nm/704 nm) post sonication. This fluorescent dye was chosen to reduce nonspecific tissue fluorescence. Excess unbound dye was removed by washing the labeled ND five times in Milli-Q water by centrifugation.

The ND-treated animals were anesthetized by isoflurane and whole animal imaging was performed at an excitation wavelength of 682 nm and an emission wavelength of 704 nm on day 12 (4 h post 4^{th} injection) and day 20 (24 h post 6^{th} injection). Post live imaging, the mice were euthanized using CO_2 followed by cervical dislocation. The heart, lung, spleen, kidney, liver, brain, and tumor were harvested and imaged for Rh800 fluorescence signal using IVIS. The

fluorescence was represented as radiance efficiency quantified using the Living Image software. The signal from each organ was normalized to the radiance efficiency of control PBS samples using the same software.

Tissue Sectioning. The organs collected post IVIS imaging were fixed overnight in 4% paraformaldehyde, followed by overnight cryoprotection in sucrose (15% w/v in 1× PBS). Post fixation and cryoprotection, the samples were frozen and embedded in optimal cutting temperature compound. The frozen samples were cut into 10 μm sections using a Leica CM1950 cryostat (Leica Biosystems) and lifted onto a positively charged Superfrost Plus adhesion glass slide. A minimum of 12 sections were collected per organ and stored at −80 °C.

Histological Imaging. Frozen and sectioned tissue samples were thawed for 10 min and washed thrice with 1× PBS in histochemistry staining boxes. The washed tissues were permeabilized using triton X (0.2%) for 10 min and washed thrice with 1× PBS. Following permeabilization, samples were incubated for 30 min in BSA (2.5% w/v in 1× PBS) to block nonspecific binding. All the above steps were performed at room temperature. Next, the samples were incubated with 1:100 times diluted anti-collagen type I (rabbit) primary antibodies (prepared in 2.5% BSA) overnight at 4 °C or 2 h at room temperature. After incubation, the samples were washed in 1× PBS and incubated in AF488-conjugated goat anti-rabbit secondary antibodies (1:500 in PBS) for 1 h at room temperature. One tissue section in each sample was stained with AF488-WGA to label the cell membranes. The nuclei in all samples were counter stained with Hoechst (1:10000, 10 min at room temperature). Samples were rinsed with 1× PBS to remove excess dye.

The sectioned samples were also stained with H&E using a kit purchased from MedChemExpress. The slides were thoroughly washed with 1× PBS five times for 3 min and stained with hematoxylin for 3 min, which binds to the negatively charged chromatins in the

nucleus. Post incubation, slides were washed in running tap water to remove excess stain. Following the wash step, the slides were dehydrated sequentially using 50–70–96% ethanol and incubated in eosin for 2 min. Then, the slides were washed in absolute ethanol thrice and the tissues were eventually cleared by incubating in xylene for 1 min. The stained tissues were mounted using mounting media onto coverslip and dried overnight.

TUNEL Assay. The presence of tissue damage was evaluated using a TUNEL assay, an indicator of apoptosis in fixed tissues. The cryosectioned samples were rinsed with 1× PBS and immersed in 4% paraformaldehyde fixative for 15 min. 1X proteinase K (400–500 µL) was added to permeabilize the tissues for 15 min and the tissues were rinsed again in 1× PBS. All of the above steps were performed at room temperature. Fixed and permeabilized samples were treated with Click-iT TUNEL assay, AF488 for apoptosis detection. TdT reactions and Click-iT reactions were performed at 37 °C using manufacturer's protocol. The samples were counter stained with Hoechst (1:10000, 10 min at room temperature) to label the nucleus.

Statistical Analysis. All data points were presented as average ± standard deviation. Correlation plots were generated using ImageJ software.

Minimum Information Reporting in Bio–Nano Experimental Literature (MIRIBEL). The studies conducted herein, including material characterization, biological characterization, and experimental details, conform to the MIRIBEL reporting standard for bio–nano research,[46] and we include a companion checklist of these components in the Supporting Information.

ASSOCIATED CONTENT

Supporting Information. Flow cytometry gating strategy; HPLC chromatograms of ND_{Dox}, ND_{Mcl1}, $ND_{Vtx+Dox}$, and $ND_{Vtx+Mcl1}$; LC/MS data of $ND_{Vtx+Dox}$; DLS, SEM, and HPLC data to study effect of varying drug mass ratios, stability, cytotoxicity, and ND internalisation; *in vivo*

whole mouse imaging of the biodistribution of free Rh800 dye in healthy mice; immunohistochemistry, H&E staining and TUNEL assays on fixed tumor tissues; and MIRIBEL checklist for reporting in bio–nano experimental literature.

AUTHOR INFORMATION

Corresponding Author

*fcaruso@unimelb.edu.au

*christina.cortez@unimelb.edu.au

Notes

The authors declare no competing interest.

ACKNOWLEDGMENT

This research was funded in part by the National Health and Medical Research Council (GNT2016732, F.Caruso). This work was also supported by the Australian Research Council under a Discovery Project scheme (F.Cavalieri, C.C.-J., DP210101792). This work was performed in part at the MCFP, the Victorian Node of the Australian National Fabrication Facility (ANFF), and the Peter Doherty Institute for Infection and Immunity. SEM analysis and LC/MS experiments were conducted at the Bio21 Advanced Microscopy Facility at the University of Melbourne. We thank Dr Karen Alt (Monash University) and Dr Jingqu Chen (University of Melbourne) for helpful discussions. The schematics in Figures 1a, 2d, 4a, 6a, 6d, 7a, 7b and the table of content graphic were created with BioRender.com.

REFERENCES

1. Zhang, J.; Hu, F.; Aras, O.; Chai, Y.; An, F. Small Molecule-Drug Conjugates: Opportunities for the Development of Targeted Anticancer Drugs. *Chem. Med. Chem.* **2024**, *19*, e202300720.

2. Kidane, A.; Bhatt, P. P. Recent Advances in Small Molecule Drug Delivery. *Curr. Opin. Chem. Biol.* **2005**, *9*, 347–351.

3. Shen, J.; Lu, Z.; Wang, J.; Zhang, T.; Yang, L.; Li, Yan.; Liu, G.; Zhang, X. Advances of Nanoparticles for Leukemia Treatment. *ACS. Biomater. Sci. Eng.* **2020**, *6*, 6478–6489.

4. McNerney, M. P.; Styczynski, M. P. Small Molecule Signaling, Regulation, and Potential Applications in Cellular Therapeutics. *Wiley. Interdiscip. Rev.: Syst. Biol. Med.* **2018**, *10*, e1405.

5. Anderson, M. A.; Deng, J.; Seymour, J. F.; Tam, C.; Kim, S. Y.; Fein, J.; Yu, L.; Brown, J. R.; Westerman, D.; Si, E. G.; Majewski, I. J.; Segal, D.; Enschede, S. L. H.; Huang, D. C. S.; Davids, M. S.; Letai, A.; Roberts, A. W. The BCL2 Selective Inhibitor Venetoclax Induces Rapid Onset Apoptosis of CLL Cells in Patients *Via* a TP53-Independent Mechanism. *Blood.* **2016**, *127*, 3215–3224.

6. Chatzikalil, E.; Roka, K.; Diamantopoulos, P. T.; Rigatou, E.; Avgerinou, G.; Kattamis, A.; Solomou, E. E. Venetoclax Combination Treatment of Acute Myeloid Leukemia in Adolescents and Young Adult Patients. *J. Clin. Med.* **2024**, *13*, 38610812.

7. Liu, J.; Chen, Y.; Yu, L.; Yang, L. Mechanisms of Venetoclax Resistance and Solutions. *Front. Oncol.* **2022**, *12*, 1005659.

8. Roberts, A. W.; Stilgenbauer, S.; Seymour, J. F.; Huang, D. C. S. Venetoclax in Patients with Previously Treated Chronic Lymphocytic Leukemia. *Clin. Cancer. Res.* **2017**, *23*, 4527–4533.

9. Shim, G. S.; Manandhar, S.; Shin, D. H.; Kim, T. H.; Kwak, M. K. Acquisition of Doxorubicin Resistance in Ovarian Carcinoma Cells Accompanies Activation of the NRF2 Pathway. *Free Radical Biol. Med.* **2009**, *47*, 1619–1631.

10. Cao, C.; Pei, Y.; Yu, H.; Qi, H. Dual Targeting Bcl-2 and Bcl-xL Augments Osteosarcoma Response to Doxorubicin. *J. Chemother.* **2024**, *36*, 156–166.

11. Bala Tannan, N.; Manzari, M. T.; Herviou, L.; Ferreira, M. D. S.; Hagen, C.; Kiguchi, H.; Manova-Todorova, K.; Seshan, V.; de Stanchina, E.; Heller, D. A.; Younes, A. Tumor-Targeted Nanoparticles Improve the Therapeutic Index of BCL2 and MCL1 Dual Inhibition. *Blood.* **2021**, *137*, 2057–2069.

12. Arandjelovic, P.; Kim, Y.; Cooney, J. P.; Preston, S. P.; Doerflinger, M.; McMahon, J. H.; Garner. S. E.; Zerbato, J. M.; Roche, M.; Tumpach, C.; Ong, J.; Sheerin, D.; Smyth, G. K.; Anderson, J. L.; Allison, C. C.; Lewin, S. R.; Pellegrini, M. Venetoclax, Alone and in Combination with the BH3 Mimetic S63845, Depletes HIV-1 Latently Infected Cells and Delays Rebound in Humanized Mice. *Cell. Rep. Med.* **2023**, *4*, 101178.

13. Wan, X.; Min, Y.; Bludau, H.; Keith, A.; Sheiko, S. S.; Jordan, R.; Wang, A. Z.; Sokolsky-Papkov, M.; Kabanov, A. V. Drug Combination Synergy in Worm-Like Polymeric Micelles Improves Treatment Outcome for Small Cell and Non-Small Cell Lung Cancer. *ACS. Nano.* **2018**, *12*, 2426–2439.

14. Zhou, L.; Li, Y.; Liang, Q.; Liu, J.; Liu, Y. Combination Therapy Based on Targeted Nano Drug Co-Delivery Systems for Liver Fibrosis Treatment: A Review. *J. Drug. Targeting* **2022**, *30*, 577–588.

15. Park, H.; Otte, A.; Park, K. Evolution of Drug Delivery Systems: From 1950 to 2020 and Beyond. *J. Controlled Release.* **2022**, *342*, 53–65.

16. Barenholz, Y. Doxil^{R}—The First FDA-Approved Nano-Drug: Lessons Learned. *J. Controlled Release.* **2012**, *160*, 117–134.

17. Din, F. U.; Aman, W.; Ullah, I.; Qureshi, O. S.; Mustapha, O.; Shafique, S.; Zeb, A. Effective Use of Nanocarriers as Drug Delivery Systems for the Treatment of Selected Tumors. *Int. J. Nanomed.* **2017**, *12*, 7291–7309.

18. Larraneta, E.; Stewart, S.; Ervine, M.; Al-Kasasbeh, R.; Donnelly, R.F. Hydrogels for Hydrophobic Drug Delivery. Classification, Synthesis and Applications. *J. Funct. Biomater.* **2018**, *9*, 13.

19. Kalepu, S.; Nekkanti, V. Insoluble Drug Delivery Strategies: Review of Recent Advances and Business Prospects. *Acta. Pharm. Sin. B.* **2015**, 5, 442–453.

20. Wang, Q.; Atluri, K.; Tiwari, A. K.; Babu, R. J. Exploring the Application of Micellar Drug Delivery Systems in Cancer Nanomedicine. *Pharmaceuticals* **2023**, *16*, 433.

21. Bharti, C.; Nagaich, U.; Pal, A. K.; Gulati, N. Mesoporous Silica Nanoparticles in Target Drug Delivery System: A Review. *Int. J. Pharm. Invest.* **2015**, *5*, 124–133.

22. Farokhzad, O. C.; Langer, R. Impact of Nanotechnology on Drug Delivery. *ACS Nano.* **2009**, *3*, 16–20.

23. Kamaly, N.; Xiao, Z.; Valencia, P. M.; Radovic-Moreno, A. F.; Farokhzad, O. C. Targeted Polymeric Therapeutic Nanoparticles: Design, Development and Clinical Translation. *Chem. Soc. Rev.* **2012,** *41*, 2971–3010.

24. Rocha, C. V.; Gonçalves, V.; da Silva, M. C.; Bañobre-López, M.; Gallo, J. PLGA-Based Composites for Various Biomedical Applications. *Int. J. Mol. Sci.* **2022**, *23*, 2034.

25. Bhangu, S. K.; Fernandes, S.; Beretta, G. L.; Tinelli, S.; Cassani, M.; Radziwon, A.; Wojnilowicz, M.; Sarpaki, S.; Pilatis, I.; Zaffaroni, N.; Forte, G.; Caruso, F.; Ashokkumar, M.; Cavalieri, F. Transforming the Chemical Structure and Bio-Nano Activity of Doxorubicin by Ultrasound for Selective Killing of Cancer Cells. *Adv. Mater.* **2022**, *34*, e2107964.

26. Szebeni, J.; Simberg, D.; Gonzalez-Fernandez, A.; Barenholz, Y.; Dobrovolskaia, M. A. Roadmap and Strategy for Overcoming Infusion Reactions to Nanomedicines. *Nat. Nanotechnol.* **2018**, *13*, 1100–1108.

27. Vega-Villa. K. R.; Takemoto. J. K.; Yanez. J. A.; Remsberg. C. M.; Forrest. M. L.; Davies, N. M. Clinical Toxicities of Nanocarrier Systems. *Adv. Drug Deliver Rev.* **2008**, *60*, 929–938.

28. Sharma. S.; Parveen. R.; Chatterji. B. P. Toxicology of Nanoparticles in Drug Delivery. *Curr. Pathobiol. Rep.* **2021**, *9*, 133–144.

29. Cheng, J.; Zhao, H.; Wang, J.; Han, Y.; Yang, X. Bioactive Natural Small Molecule-Tuned Coassembly of Photosensitive Drugs for Highly Efficient Synergistic and Enhanced Type I Photochemotherapy. *ACS Appl. Mater. Interfaces* **2020**, *12*, 43488–43500.

30. Gigliobianco, M. R.; Casadidio, C.; Censi, R.; Di Martino, P. Nanocrystals of Poorly Soluble Drugs: Drug Bioavailability and Physicochemical Stability. *Pharmaceutics* **2018**, *10*, 134.

31. Kakran, M.; Shegokar, R.; Sahoo, N. G.; Gohla, S.; Li, L.; Muller, R. H. Long-Term Stability of Quercetin Nanocrystals Prepared by Different Methods. *J. Pharm. Pharmacol.* **2012**, *64*, 1394–1402.

32. Chen, S.; Fan, J. X.; Liu, X. H.; Zhang, M. K.; Liu, F.; Zeng, X.; Yan, G. P.; Zhang, X. Z. A Self-Delivery System Based on an Amphiphilic Proapoptotic Peptide for Tumor Targeting Therapy. *J. Mater. Chem. B.* **2019**, *7*, 778–785.

33. Mei, H.; Cai, S.; Huang, D.; Gao, H.; Cao, J.; He, B. Carrier-Free Nanodrugs with Efficient Drug Delivery and Release for Cancer Therapy: From Intrinsic Physicochemical Properties to External Modification. *Bioact. Mater.* **2022**, *8*, 220–240.

34. Jiang, S.; Fu, Y.; Zhang, X.; Yu, T.; Lu, B.; Du, J. Research Progress of Carrier-Free Antitumor Nanoparticles Based on Phytochemicals. *Front. Bioeng. Biotechnol.* **2021**, *9*, 799806.

35. Mei, H.; Cai, S.; Huang, D.; Gao, H.; Cao, J.; He, B. Carrier-Free Nanodrugs with Efficient Drug Delivery and Release for Cancer Therapy: From Intrinsic Physicochemical Properties to External Modification. *Bioact. Mater.* **2022**, *8*, 220–240.

36. Jiang, S.; Fu, Y.; Zhang, X.; Yu, T.; Lu, B.; Du, J. Research Progress of Carrier-Free Antitumor Nanoparticles Based on Phytochemicals. *Front. Bioeng. Biotechnol.* **2021**, *9*, 799806.

37. Bhangu, S. K.; Bocchinfuso, G.; Ashokkumar, M.; Cavalieri, F. Sound-Driven Dissipative Self-Assembly of Aromatic Biomolecules into Functional Nanoparticles. *Nanoscale Horiz.* **2020**, *5*, 553–563.

38. Cavalieri, F.; Colombo, E.; Nicolai, E.; Rosato, N.; Ashokkumar, M. Sono-Assembly of Nanostructures Tyrosine-Tyrosine Coupling Reactions at the Interface of Acoustic Cavitation Bubbles. *Mater. Horiz.* **2016**, *3*, 563–567.

39. Bhangu, S. K.; Baral, A.; Zhu, H.; Ashokkumar, M.; Cavalieri, F. Sound Methods for the Synthesis of Nanoparticles from Biological Molecules. *Nanoscale Adv.* **2021**, *3*, 4907–4917.

40. Baral, A.; Bhangu, S. K.; Cimino, R.; Pelin J. N. B. D.; Alves, W. A.; Chattopadhyay, S.; Ashokkumar, M.; Cavalieri, F. Sono-Assembly of the $[Arg\text{-}Phe]_4$ Octapeptide into Biofunctional Nanoparticles. *Nanomaterials.* **2020**, *10*, 1772.

41. Bhangu, S. K.; Singla, R.; Colombo, E.; Ashokkumar, M.; Cavalieri, F. Sono-Transformation of Tannic Acid into Biofunctional Ellagic Acid Micro/Nanocrystals with Distinct Morphologies. *Green Chem.* **2018**, *20*, 816–821.

42. Zhu, H.; Wen, Q.; Bhangu, S. K.; Ashokkumar, M.; Cavalieri, F. Sonosynthesis of Nanobiotics with Antimicrobial and Antioxidant Properties. *Ultrason. Sonochem.* **2022**, *86*, 106029.

43. Perdih, F.; Zigart, N.; Casar, Z. Crystal Structure and Solid-State Conformational Analysis of Active Pharmaceutical Ingredient Venetoclax. *Crystals* **2021**, *11*, 261.

44. Yin, L.; Zeng, Y.; Zeng, R.; Chen, Y.; Wang, T. L.; Rodabaugh, K. J.; Yu, F.; Natarajan, A.; Karpf, A. R.; Dong, J. Protein Kinase RNA-Activated Controls Mitotic Progression and Determines Paclitaxel Chemosensitivity Through B-Cell Lymphoma 2 in Ovarian Cancer. *Oncogene* **2021**, *40*, 6772–6785.

45. Sheth, V.; Wang, L.; Bhattacharya, R.; Mukherjee, P.; Wilhelm, S. Strategies for Delivering Nanoparticles Across Tumor Blood Vessels. *Adv. Funct. Mater.* **2021**, *31*, 2007363.

46. Faria, M.; Bjornmalm, M.; Thurecht, K. J.; Kent, S. J.; Parton, R. G.; Kavallaris, M.; Johnston, A. P. R.; Gooding, J. J.; Corrie, S. R.; Boyd, B. J.; Thordarson, P.; Whittaker, A. K.; Stevens, M. M.; Prestidge, C. A.; Porter, C. J. H.; Parak, W. J.; Davis, T. P.; Crampin, E. J.; Caruso, F. Minimum Information Reporting in Bio–Nano Experimental Literature. *Nat. Nanotechnol.* **2018**, *13*, 777–785.

Table of content graphic